PREPARED FOR THE U.S. DEPARTMENT OF ENERGY,
UNDER CONTRACT DE-AC02-76-CHO-3073

PPPL-2794
UC-427

PPPL-2794

STRUCTURE OF THE MAGNETOPAUSE CURRENT LAYER AT THE SUBSOLAR POINT

BY

H. OKUDA

December 1991

PPPL PRINCETON PLASMA PHYSICS LABORATORY

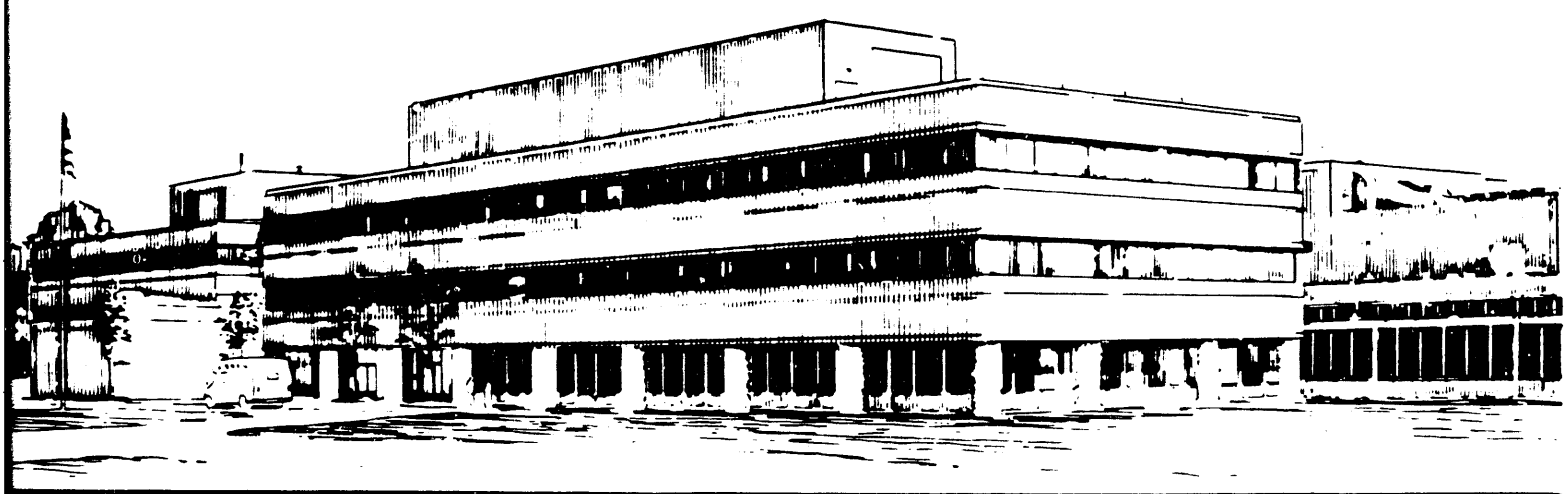

PRINCETON UNIVERSITY, PRINCETON, NEW JERSEY

NOTICE

NOTICE

PPPL--2794

DE92 003993

Structure of the Magnetopause Current Layer at the Subsolar Point

H. Okuda

Princeton Plasma Physics Laboratory, Princeton University

Princeton, NJ 08543

Abstract

A one-dimensional electromagnetic particle simulation model developed for the magnetopause current layer between the shocked solar wind and the dipole magnetic field at the subsolar point has been extended to include the interplanetary magnetic field (IMF) in the solar wind. Interaction of the solar wind with the vacuum dipole field as well as the dipole field filled with a low density magnetospheric plasma are studied. It is found that the width and the structure of the magnetopause current layer differ markedly depending on the direction of the IMF. When the IMF is pointing southward, the current layer between the solar wind and the dipole field is narrow and the magnetic field has a single ramp structure caused by the reflection of the solar wind at that point. The current layer becomes several times wider and the magnetic field develops a multiple ramp structure when the IMF is northward. This broadening of the current layer is caused by the multiple reflection of the solar wind by the magnetic field. For the northward IMF, the magnetic field does not change its sign across the current layer so that the $E \times B$ drift of the solar wind electrons remains the same direction while for the southward IMF, it reverses the sign. This results in a single reflection of the solar wind for the southward IMF and multiple reflections for the northward IMF. When a low density magnetospheric plasma is present in the dipole magnetic field, a small fraction of the solar wind ions are found to penetrate into the dipole magnetic field beyond the reflection point of the solar wind electrons. The width of the ion

current layer is of the order of the solar wind ion gyroradius, however, the current associated with the ions remains much smaller than the electron current so long as the density of the magnetospheric plasma is much smaller than the density of the solar wind. Comparisons of our simulation results with the recent spacecraft data of the magnetopause crossing near the subsolar point are provided.

I. Introduction

Structure of the magnetopause boundary layer near the subsolar point of the earth has been studied extensively by means of analytic theory (Longmire, 1963; Sestero, 1964, 1965; Lee and Kan, 1979), spacecraft observations (Russell and Elphic, 1978; Berchem and Russell, 1982; Haerendel and Paschmann, 1982; Paschmann, 1984; Elphic, 1987; Song et al., 1989, 1990) and numerical simulations (Berchem and Okuda, 1990; Okuda, 1990). Using the unmagnetized cold solar wind model in which the random thermal motions of the particles are small in comparison with the macroscopic drift speed of the plasma flowing normal to the magnetic field, the width of the current layer between the solar wind and the magnetic field is given by the hybrid gyroradius δ defined by

$$\delta = (\rho_e \rho_i)^{1/2} \tag{1}$$

where ρ_e and ρ_i are the electron and ion gyroradii at the reflection point defined by $\rho_{e,i} = V_o/\Omega_{e,i}$ (Longmire, 1963). Here V_o is the drift speed and $\Omega_{e,i} \equiv eB/m_{e,i}c$ is the gyrofrequency. The width given by Eq. (1) is much smaller than the ion gyroradius because the ions are tied to the electrons by the electric field caused by the charge separation at the current layer. The width given Eq. (1) is equal to the skin depth $\delta = c/\sqrt{2}\ \omega_{pe}$ if the pressure balance between the plasma and the magnetic field

$$m_i n_{sw} V_o^2 = B^2/8\pi \tag{2}$$

is used. Here n_{sw} is the solar wind particle density and ω_{pe} is the electron plasma frequency.

The result of Eq. (1) cannot be applied directly to the magnetopause boundary layer at the subsolar point since the shocked solar wind flow speed is subsonic rather than supersonic after passing the bow shock. Extensive one-dimensional electromagnetic particle code simulations, however, confirmed that even for a subsonic flow the main point of Eq. (1) remains valid verifying the width of the current layer is essentially given by the hybrid gyroradius (Okuda, 1990). Furthermore, it was shown that the narrow current layer persists even in the presence of a magnetospheric plasma in the dipole magnetic field. A presence of such an ambient plasma neutralizes the charge separation at the current layer thereby allowing the solar wind ions to penetrate deeper into the dipole magnetic field. The width of the ion current layer is of the order of the solar wind ion gyroradius. So long as the magnetospheric plasma density is smaller than the solar wind density at the subsolar point (Song et al., 1989), however, the current associated with the ions remains small since the density of the solar wind ions penetrating into the magnetospheric side is limited to the magnetospheric ion density (Okuda, 1990). Thus, in this case, the current layer is dominated by the diamagnetic current given by

$$\underset{\sim}{J}_D = \frac{-\nabla p \times \underset{\sim}{B}}{B^2}, \tag{3}$$

in addition to the electrons $\underset{\sim}{E} \times \underset{\sim}{B}$ current so that the width remains much smaller than the ion gyroradius (Okuda, 1990).

While the above-mentioned works are interesting and important in their own right, the solar wind is rarely unmagnetized and is filled with the IMF. It is well known that the direction of the IMF is important in determining the solar wind transfer into the magnetosphere. In addition, the structure of the boundary layer near the subsolar point appears to depend on the direction of the IMF (Song et al., 1989).

In this paper, the one-dimensional electromagnetic particle code for the magnetopause current layer is extended to include the IMF in the solar wind. Both the southward and northward pointing IMFs are considered and compared with the earlier result in the absence of the IMF. We found that for the southward IMF the current layer remains narrow and single-ramped similar to the case where no IMF existed. For the case of the northward IMF, the current layer becomes several times wider and is associated with multiple ramp structure. We found the structure of the current layer is caused by the multiple reflection of the solar wind. Comparisons with the spacecraft data available at the subsolar point are discussed.

In Sec. II, the simulation model was discussed briefly. Results of the simulations are given for the cases with no IMF in Sec. III, southward IMF in Sec. IV, and northward IMF in Sec. V. Comparisons of the simulation results with the spacecraft data and discussions are given in Sec. VI.

II. Simulation Model

Consider a one-dimensional plasma model in a magnetic field as sketched in Fig. 1. The dipole magnetic field is approximated by a straight magnetic field given by

$$B_z(x)/B_o = -\frac{1}{(x/x_D - 1)^3} \quad \text{for } 0 \le x \le L\,, \tag{4}$$

where x_D is the location of the dipole and L is the length of the simulation model. Similar magnetic field model was used earlier (Hasegawa and Okuda, 1967; Okuda, 1990). Note the magnetic field given by Eq. (4) is not curl free so that a current is needed to generate

such a magnetic field. The real dipole field is curl free except for at the origin, however, a current is needed to straighten the curvature for the present one-dimensional model. In the simulation results reported here, the d.c. current necessary to produce the dipole field B_z was assumed frozen so that it was not shown in the figures. The width of the current layer is of the order of the hybrid gyroradius much smaller than the ion gyroradius so that a straight magnetic field approximation may be justified. Typically $x_D = 1.5$ L was chosen in the simulations, however, the width and the structure of the current layer is independent of x_D so long as it is much larger than the hybrid gyroradius (Berchem and Okuda, 1990).

A low density magnetospheric plasma may be present in the dipole magnetic field. The density of such a plasma is chosen smaller than the shocked solar wind density, typically at (10-20%), and its temperature is chosen higher than the solar wind temperature, typically 10 times or so, in accordance with space observations (Song et al., 1989).

The solar wind is initially located at $x \leq 0$ whose distribution is given by

$$f_{e,i} = \frac{n_{sw}}{2\pi\, v_{te,i}} \exp\left[-\frac{(v - v_o)^2}{2v_{te,i}^2}\right], \tag{5}$$

for the ions and electrons. Typically $T_i/T_e = 9$, $m_i/m_e = 400$, and $V_o/v_{ti} = 0.8$ are used for the solar wind.

A full electromagnetic particle code was used throughout the numerical simulations (Lin et al., 1975) instead of a magnetostatic code which neglects the transverse displacement current (Hasegawa and Okuda, 1967). Full Maxwell's equations are solved by using a finite difference method in x using the boundary values at $x = 0$ and $x = L$. In particular, $\underline{B} = (B_y, B_z)$ at $x = 0$ are chosen such that the solar wind magnetic field has the

prescribed interplanetary magnetic field. Similarly, the transverse electric fields $\underset{\sim}{E}^T = (E_y, E_z)$ at x = L are determined from the macroscopic velocity of the electrons, $\underset{\sim}{E}^T = -\underset{\sim}{v}_e \times \underset{\sim}{B}/c$ which is appropriate for the low frequency convection electric field. The boundary condition for the longitudinal electric field $E^L = E_x$ is chosen 0 at x = L assuring no charge separation existed away from the current layer. Similar boundary conditions have been used in our earlier publications (Hasegawa and Okuda, 1967; Berchem and Okuda, 1990; Okuda, 1990).

Typically we chose the system length L = 1024 Δ where Δ is the grid space which is equal to the solar wind electron Debye length. One hundred simulation particles per grid are used for the solar wind electrons and ions. The number of particles for the magnetospheric plasma is smaller by the density ratio determined at the beginning of the simulations. The strength of the magnetic field, (4), at x = 0, B_0 is chosen such that the electron gyrofrequency $\Omega_e = 0.2\ \omega_{pe}$ where $\omega_{pe} \equiv (4\pi n_{sw} e^2/m_e)^{1/2}$ is the solar wind electron plasma oscillation. The corresponding gyroradii of the electrons and ions are typically $\rho_e \equiv V_o/\Omega_e = 0.6\ \Delta$ and $\rho_i = V_o/\Omega_i = 240\ \Delta$, respectively. The ion thermal velocity was typically $v_{ti} = 0.8\ V_0$ consistent with the shocked solar wind. The corresponding plasma $\beta \equiv nT/(B^2/8\pi)$ was 5 or 20 for x < 0 depending on the choice of B_0. In all the simulations reported here, the ion-electron mass ratio $m_i/m_e = 400$ was used.

III. Simulation Results Without IMF

Let us first describe the results of the simulations where the IMF is negligibly small in the solar wind. Observationally such a case is rare, however, from the theoretical point of view, this is the only case one can find an analytic solution for the current layer problem (Longmire, 1963). Results from the two runs will be shown. The first (case 1) is the

injection of the solar wind into the vacuum magnetic field. In the second (case 2), the dipole field is filled with a low density and high temperature magnetospheric plasma.

Figure 2 summarizes the first simulation (case 1) where $\Omega_e/\omega_{pe} = 0.2$ and $V_o/v_{te} = 0.12$ at $\omega_{pe}t = 2000$ when the system reached more or less a time-independent steady state. The (x, v_x) phase space plots of the solar wind electrons, Fig. 2(a), and ions Fig. 2(b) indicate that the solar wind is reflected near $x = 250\ \Delta$ creating a magnetic field ramp as shown in Fig. 2(c) for the solar wind generated magnetic field and in Fig. 2(d) for the total magnetic field. The sharp current layer is readily visible in Fig. 2(e) showing the J_y current. The electrostatic potential which confines the ions at the current layer is shown in Fig. 2(f).

Using the pressure balance, [Eq. (2)], and the prescribed magnetic field, [Eq. (4)], the reflection point is found to be approximately $250\ \Delta$ in good agreement with the simulation. The dipole magnetic field is swept by the unmagnetized solar wind so that there is no magnetic field in the solar wind as shown in Fig. 2(d). Both the induced magnetic field, Fig. 2(c), and the total magnetic field, Fig. 2(d), show a sharp ramp structure whose width δ is about $\delta = 25\ \Delta$ measured at one half of the J_y current. Note the electron gyroradius $\rho_e = V_o/\Omega_e = 0.6\ \Delta$ and ion gyroradius $\rho_i = V_o/\Omega_i = 240\ \Delta$ so that $(\rho_e\rho_i)^{1/2} \approx 24\ \Delta$. It is clear that the observed width of the boundary layer is much larger than ρ_e and much smaller than ρ_i. The potential jump is $e\phi/T_i \approx 10$ suggesting that it is determined by the high energy tail ions (Okuda, 1990).

In order to study the effect of the magnetospheric plasma on the boundary layer, a low density, high temperature ambient plasma is added in the dipole field (case 2). The ambient density n_{ms} and the temperature T_{ms} are initially taken $n_{ms} = 0.1\ n_{sw}$ and $T_{ms} = 10$

T_e where T_e is the solar wind electron temperature (Song et al., 1990). The density of the magnetospheric plasma is uniformly distributed in the dipole field for

$$8/L \leq x \leq (7/8)\, L\,. \tag{6}$$

We note that the magnetospheric ions are electrostatically confined in the magnetic field. The dipole field in this simulation is reduced by a factor of 2 from the first simulation so that $\Omega_e/\omega_{pe} = 0.1$ at $x = 0$. This allows deeper penetration of the solar wind as we shall see next.

As the solar wind plasma sweeps the dipole magnetic field, magnetospheric electrons are compressed along with the magnetic field. This is because the electron gyroradius is small so that they are tied to their own magnetic field (frozen-in condition). The ion gyroradius is large, a few hundred grid space, so that they are not frozen-in their field on the scale length of the current layer. This will allow the solar wind and the magnetospheric ions to mix together at a distance of the order of the gyroradius (Okuda, 1990).

Figure 3 shows the results of the simulation at $\omega_{pe}t = 2500$ for the Fig. 3(a) magnetospheric ion density n^i_{ms}, Fig. 3(b) magnetospheric electron density n^e_{ms}, Fig. 3(c) solar wind ion density n^i_{sw}, and the solar wind electron density Fig. 3(d). Here n_o is the solar wind density at $x < 0$. It is clear that the magnetospheric ions leak toward the solar wind while the magnetospheric electrons are tied to the dipole magnetic field compressed by the solar wind as shown in Figs. 3(a) and (b). Similarly, the solar wind ions leaked into the magnetosphere Fig. 3(c), while the solar wind electrons are tied to the magnetic field owing to their much smaller gyroradii as shown in Fig. 3(d). At the interface of the solar wind and the magnetospheric electrons, a sharp density discontinuity exists giving

rise to a current layer at that point (Okuda, 1990). Note the solar wind densities shown in (c) and (d) are less than one-half of n_o which is the total solar wind density at $x < 0$. This is because only those particles whose x-velocity is positive at $x < 0$ enter the simulation domain at $x > 0$. It is clear from Eq. (5) that the fraction of those electrons is about 50%. However, the ion flux must be equal to the electron flux so that a sheath electric field is set up to accelerate ions and decelerate electrons at $x = 0$. This results in the net density at $x > 0$ generally less than 50% of n_o.

Figure 4(a) represents the induced magnetic field, δB_z Fig. 4(b) total magnetic field, B_z Fig. 4(c) total current J_y and Fig. 4(d) the electrostatic potential, $e\phi/T_e$. It is clear that the reflection point moved deeper into the dipole field as expected. The width of the layer remains about the same, however, since the magnetic field at the reflection point is determined by the solar wind pressure, Eq. (2).

In the presence of a low density magnetospheric plasma, charge separation at the current layer is significantly reduced so that the current J_y, Fig. 4(c), and the electrostatic potential ϕ Fig. 4(d) are smaller than those from case 1 (Okuda, 1990). It should be emphasized, however, that the maximum amount of the solar wind ions penetrating into the magnetosphere cannot exceed the magnetospheric ion density. This is because the electrons are tied to their initial magnetic field lines (frozen-in) so that the penetration of the solar wind ions into the magnetosphere must be accompanied by the magnetospheric ion leakage to the solar wind. The fraction of the solar wind ions penetrating into the magnetosphere is, therefore, small. The current at the boundary layer, Fig. 4(c) is therefore produced in part by the diamagnetic currents in addition to the electron $E \times B$ current (Okuda, 1990) and no appreciable ion currents have been observed. The potential profile shown in Fig. 4(d) indicate a wavy structure instead of a single ramp structure seen

in Fig. 2(f) suggesting a neutralization process of the charge-separation by the magnetospheric plasma.

IV. Simulation Results with the Southward IMF

Next we consider the cases where the solar wind has a southward IMF. This was achieved by choosing the solar wind magnetic field B_z at x = 0 negative such as $B_z = -B_o$ while the convection electric field E_y is determined as before. Note the convection electric field is induced self-consistently by the motion of the solar wind across magnetic field at x = 0 which is carried into the dipole magnetic field by the solar wind. In this way, it is not necessary to assume, for example, $E_y = B_z V_o/c$ at x = 0 which is valid only when the gyroradii of the ions and electrons are much smaller than the scale length of our interest (MHD approximation). Such a condition does not hold in the present case.

Figure 5 indicates the case (case 3) at $\omega_{pe}t = 2000$ where $B_{IMF} = -B_o$ in the presence of the same low density magnetospheric plasma as in case 2. B_o is the same as in case 1. Shown are the Fig. 5(a) solar wind ion density, n^i_{sw}, Fig. 5(b) total current J_y, Fig. 5(c) magnetic field, B_z, and Fig. 5(d) the convection electric field, E_y. The solar wind ion density, Fig. 5(a), is similar to the electron density (not shown) except for the ion tail population penetrating deep into the dipole field as before. The current J_y is again very sharp with the width about the same as before and it is determined by the electrons with negligible ion component. The magnetic field, Fig. 5(c), is southward for small x until it jumps to the dipole field at the current layer near x = 250 Δ. The self-consistent convection electric field, Fig. 5(d), is induced and is negative, $E_y < 0$, so that the cE_y/B_z gives a positive flow speed for $B_z < 0$ in agreement with the direction of the solar wind injection. Numerically its value is found to be close to, but smaller than, the convection field determined from the injection speed of the solar wind ($c E_y/B_z = 0.85 V_o$). Note again it is

not surprising here that the MHD approximation, $\underset{\sim}{E} + \underset{\sim}{v} \times \underset{\sim}{B}/c = 0$, does not necessarily hold here. The convection field becomes zero beyond the reflection point as expected.

Shown in Fig. 6 is the case (case 4) where the IMF is strongly southward $B_{IMF} = -3B_0$. The magnetic field Fig. 6(a) shows a clear sharp ramp at the current layer. The reflection point moved deeper into the dipole field in this case as expected since the solar wind has a larger magnetic field pressure. The (x, v_x) phase space for the solar wind ions, Fig. 6(b), indicates that part of the solar wind ions penetrating into the magnetosphere. These solar wind ions are eventually reflected back toward the injection point.

From these simulations, it is clear that the solar wind with a southward IMF carries its magnetic field while sweeping the dipole magnetic field until the solar wind reaches the reflection point (current layer). Beyond the current layer the magnetic field smoothly follows the dipole magnetic field. The width of the boundary layer is much narrower than the ion gyroradius and much wider than the electron gyroradius and is close to the hybrid gyroradius. These features are close to those found for the unmagnetized solar wind discussed in Sec. III. Note the magnetic field changes its sign across the current layer from negative to positive so that the solar wind electrons cannot cross the current layer since the cE_y/B drift changes its sign for the southward IMF. More will be discussed on this point in the next section.

V. Simulation Results with the Northward IMF

Now we consider a case (case 5) where the IMF is northward so that it is in the same direction as the dipole field. The parameters of these simulations are the same as in the previous simulations (cases 1, 3, 4) except for the choice of the IMF. Figures 7 and 8 show the results of case 5 where $B_{IMF} = 2\ B_0$. Initially the magnetospheric density is

again 10% of the solar wind density and its temperature is 10 times that of the solar wind electrons as before. The magnetospheric ions, Fig. 7(a), and the electrons, Fig. 7(b), are compressed by the incoming solar wind with a small amount of the magnetospheric ion leaking into the solar wind as before. These ions are replaced by the solar wind ions leaking into the magnetosphere as shown in Fig. 7 (c). No mixing between the solar wind electrons and magnetospheric electrons takes place as seen in Fig. 7 (b) and (d), as these two kinds of electrons are tied to the IMF and the dipole magnetic field. Phase space plot of the solar wind ions, Fig. 7(e), indicate, however, that the reflection of the solar wind ions takes place in several steps (multiple reflection) in contrast to a single reflection for the case of no IMF and the southward IMF. The difference is clearly seen by comparing Fig. 7(e) with Fig. 2(b). The first reflection takes place at $x = 250\ \Delta$ which is the same location for cases 1 and 3. Instead of total reflection, part of the solar wind ions continue to penetrate into the dipole field as shown in Fig. 7(e). The second reflection takes place at $x = 450\ \Delta$ beyond which a small fraction of the solar wind ions can gyrate into the dipole magnetic field as before.

The corresponding induced magnetic field δB_z, total magnetized B_z, current density J_y and the convection electric field E_y are shown in Fig. 8 in this case 5. It is apparent that the structure of the current layer in this case is very different from all the previous cases where the IMF was zero or southward. First of all, the total magnetic field B_z, Fig. 7(b), does not have a sharp boundary layer characterized by a presence of a single ramp structure. Instead, the layer is much wider and have several ramps which are clearly seen in the induced magnetic field δB_z, Fig. 7(a). These structures correspond to the multiple reflection of the solar wind as seen in Fig. 7(e) and can be explained qualitatively in a following manner. The solar wind sweeps the dipole magnetic field for small $x \leq 200\ \Delta$ and piles it up in front of the solar wind creating a hump of the magnetic field at $x \approx 250\ \Delta$. The solar wind would have been totally reflected back if the IMF were zero or southward

as in the previous cases. In this case where the IMF is northward, however, only a partial reflection takes place at this point as evidenced in Fig. 6 (e) where only part of the solar wind ions are reflected at x = 250 Δ. Since the total magnetic field does not change its sign at this reflection point in this northward IMF case, however, the c E_y/B_z drift carries the solar wind electrons further into the dipole field beyond the first reflection point allowing the solar wind ions to follow. Note for the southward IMF, B_z changes its sign causing the electrons to reflect back to the injection point. The same process can repeat until the whole solar wind is eventually reflected. This explains the second hump of the induced magnetic field at x ≈ 450 Δ in Fig. 8 (a). At each reflection point part of the solar wind is reflected back toward the injection point. Clearly the amplitude of the current layer is smaller at each reflection point since only a partial reflection takes place. Note the convection electric field, E_y, shown in Fig. 8 (d) is positive and is continuous across the current layers as required from Maxwell's equations. The corresponding current J_y, Fig. 8 (c) is much wider, but its amplitude is smaller. Again, most of the current is carried by the electrons. Simulations using larger northward IMFs give qualitatively the same structure for the current layer.

VI. Discussions

We have shown via one-dimensional particle simulations that the structure of the magnetopause current layer is very different depending on the direction of the IMF. When the IMF is negligible or southward, the current layer is narrow with a single ramp structure in the magnetic field. The width of the layer is much smaller than the solar wind ion gyroradius, much larger than the electron gyroradius, and is close to the hybrid gyroradius. In the presence of a low density magnetospheric plasma, a small fraction of the solar wind ions can leak deep into the dipole magnetic field thereby forming a wider current layer whose width is of the order of the solar wind ion gyroradius. The current and hence the

magnetic field ramp associated with such ions remain, however, small because the fraction of the solar wind ions penetrating deeper into the magnetosphere is less than the magnetospheric ion density. The current layer and hence the ramp structure of the magnetic field is dominated by the electrons so that the width of the layer remains close to the hybrid gyroradius even in the presence of a low density magnetospheric plasma.

When the IMF is northward, we found that the current layer and the magnetic field structure becomes broader with several small structures imbedded in contrast to the southward IMF where only a single ramp structure exists. Each small structure corresponds to the sweeping of the dipole field and partial reflection of the solar wind. The reflection is not complete, however, so that the same process can repeat until the total reflection takes place. The solar wind electrons can propagate by the c E_y/B_z drift further into the dipole magnetic field after each reflection for the northward IMF. After repeating the same process several times, sweeping the magnetic field and the resultant partial reflection, the solar wind is fully reflected back toward the injection point leaving multiple ramp structures of the magnetic field. The resultant current layer is broader but its amplitude is smaller.

It is interesting to compare our simulation results with the recent ISEE observations at the subsolar magnetopause crossing (Song et al., 1989, 1990). In particular, the detailed structure of the subsolar magnetopause was compared for both the northward and the southward IMF (Song et al., 1989). The reported magnetopause structure is complicated, consisting of several regions including the magnetosheath, sheath transition layer, boundary layer, and the magnetosphere. Furthermore, there are more than one scale length in the satellite data. For our purpose of comparison, let us focus on the sharp boundary between the sheath transition layer and the boundary layer in Figs. 1 and 2 of Song et al., 1989, where the jumps in the plasma density, temperature, and magnetic field indicate it is

the current layer between the solar wind and the magnetospheric plasma This boundary layer is much narrower than the ion gyroradius and is a few hybrid gyroradius consistent with our simulation results (Song et al., 1989, 1990). Furthermore, the boundary seems to be wider and shallower for the northward IMF also in agreement with our numerical simulations. Certainly, closer comparisons of the space data with simulation results are necessary to understand the structure of the subsolar magnetopause.

While the present simulation was done only in one-dimension, two-dimensional simulations in the equatorial and meridian planes indicate a presence of plasma instabilities at the current layer. It is therefore possible for the instabilities to bring in another scale length and the structure through the plasma turbulence in addition to the hybrid gyroradius. We should also point out that the one-dimensional model does not allow the solar wind to flow along the flanks of the magnetopause which will eventually happen as the solar wind pressure goes up at the subsolar point. Much work remains to be done for understanding the structure of the real magnetopause boundary layer.

Acknowledgements

This work was supported by the National Science Foundation Grants ATM-8914792 and ATM-9111682, National Aeronautics and Space Administration Grant NAGW-2538 and the U.S. Department of Energy Contract DE-AC02-76-CHO3073 to Princeton University. Part of the computing was carried out on the Cray Y-MP at the San Diego Super Computer Center supported by the National Science Foundation.

References

Berchem, J. and H. Okuda, A two-dimensional particle simulation of the magnetopause current layer, J. Geophys. Res., 95, 8133, 1990.

Berchem, J. and C. T. Russell, The thickness of the magnetopause current layer: ISEE 1 and 2 observations, J. Geophys. Res., 87, 2108, 1982.

Elphic, R. C., The bow shock and the magnetopause, Rev. Geophys., 25, 510, 1987.

Hasegawa, A., and H. Okuda, Computer experiment on Ferraro-Rosenbluth problem, J. Phys. Soc. Japan, 23, 906, 1967.

Haerendel, G., and G. Paschmann, Interaction of the solar wind with the dayside magnetosphere, in Magnetospheric Plasma Physics, edited by A. Nishida, p. 49, D. Reidel, Hingham, Massachusetts, 1982.

Lee, L. C., and J. R. Kan, A unified kinetic model of the tangential magnetopause structure, J. Geophys. Res., 84, 6417, 1979.

Lin, A. T., J. M. Dawson, and H. Okuda, Application of electromagnetic particle simulation to the generation of electromagnetic radiation, Phys. Fluids, 17, 1995, 1975.

Longmire, C. L., Elementary Plasma Physics, 90 pp., Interscience Publications, New York, 1963.

Okuda, H., Numerical simulations on the magnetopause current layer, Princeton Plasma Physics Laboratory Report, PPPL-2729, 1990; Magnetosphere/Ionosphere Plasma Models, edited by M. D. Chandler and G. R. Wilson (Geophysical Monograph, AGU publications, 1991).

Paschmann, G., N. Sckopke, G. Haerendel, I. Papamastorakis, S. J. Bame, J. R. Asbridge, J. T. Gosling, E. W. Hones, Jr., and E. R. Tech, ISEE plasma observations near the subsolar magnetopause, Space Sci. Rev., 22, 717, 1978.

Paschmann, G., Plasma and particle observations at the magnetopause: Implication for reconnection, in Magnetic Reconnection in Space and Laboratory Plasmas, Geophys. Monogr. Ser., vol. 30, edited by E. W. Hones, Jr., p. 114, AGU, Washington, DC, 1984.

Russell, C. T., and R. C. Elphic, Initial ISEE magnetometer results: Magnetopause observations, Space Sci. Rev., 22, 681, 1978.

Sestero, A., Structure of plasma sheaths, Phys. Fluids, 7, 44, 1964

Sestero, A., Charge separation effects in the Ferraro-Rosenbluth cold plasma sheath model, Phys. Fluids, 8, 739, 1965.

Song, P., C. T. Russell, N. Lin, R. J. Strangeway, J. T. Gosling, M. Thomsen, T. A. Fritz, D. G. Mitchell, and R. R. Anderson, Wave and particle properties of the subsolar magnetopause, Physics of Space Plasmas, 463 pp., SPI Conference Proceedings and Reprint Series, #9, Scientific Publishers, Inc., Cambridge, 1989.

Song, P., R. C. Elphic, C. T. Russell, J. T. Gosling, and C. A. Cattell, Structure and properties of the subsolar magnetopause for northward IMF: ISEE observations, J. Geophys. Res., 95, 6375, 1990.

Figure Captions

Fig. 1 A sketch of the simulation model. The solar wind initially located at $x \leq 0$ are injected into the dipole magnetic field B_z at a constant rate. The magnetic field at $x = 0$ is adjusted to control the interplanetary magnetic field.

Fig. 2 Results of the simulations when the interplanetary magnetic field is zero without a magnetospheric plasma (case 1). Shown are the (a) solar wind electron phase space, $(x - v_{ex})$, (b) solar wind ion phase space, $(x - v_{ix})$, (c) perturbed magnetic field, δB_z, (d) total magnetic field, B_z and the initial dipole field, (e) current density, J_y, and (f) electrostatic potential ϕ at $\omega_{pe}t = 2000$. Note the current density shown is dimensionless defined by $J_y/en_o v_{te}$.

Fig. 3 Results of the simulation with a low density, high temperature magnetospheric plasma. No IMF (case 2). Shown are the (a) magnetospheric ion density, n^i_{ms}, (b) magnetospheric electron density, n^e_{ms}, (c) solar wind ion density, n^i_{sw}, and (d) solar wind electron density, n^e_{sw} at $\omega_{pe}t = 2500$.

Fig. 4 Results from case 2. Shown are the (a) perturbed magnetic field, δB_z, (b) total magnetic field and the initial dipole field, (c) current density, J_y and (d) the electrostatic potential, ϕ at $\omega_{pe}t = 2500$.

Fig. 5 Results of the simulation when the IMF is southward. $B_{IMF} = -B_o$ in the presence of a low density, high temperature magnetospheric plasma (case 3). Shown are the (a) solar wind ion density, n^i_{sw}, (b) current density, J_y, (c) total magnetic field, B_z and the initial dipole magnetic field, and (d) convection electric field, E_y, at $\omega_{pe}t$ = 2000.

Fig. 6 Results of the simulations when the IMF is strongly southward, $B_{IMF} = -3\ B_o$ with a low density, high temperature magnetospheric plasma (case 4). Shown are the (a) total magnetic field, B_z and the initial dipole magnetic field, and (b) the solar wind ion phase space, $(x - v_{ix})$ at $\omega_{pe}t = 2000$. Note the presence of solar wind ions penetrating deep into the magnetosphere.

Fig. 7 Results of the simulation when the IMF is northward, $B_{IMF} = 2\ B_o$ with a low density, high temperature magnetospheric plasma (case 5). Shown are the (a) magnetospheric ion density, n^i_{ms}, (b) magnetospheric electron density, n^e_{ms}, (c) solar wind ion density, n^i_{sw}, (d) solar wind electron density, n^e_{sw}, (e) solar wind ion phase space, $(x - v_{ix})$ and (f) solar wind electron phase space, $(x - v_{ex})$ at $\omega_{pe}t = 2750$.

Fig. 8 Results from case 5. Shown are the (a) induced magnetic field, δB_z, (b) total magnetic field, B_z and the initial dipole field, (c) total current, J_y, and (d) convection electric field, E_y at $\omega_{pe}t = 2750$.

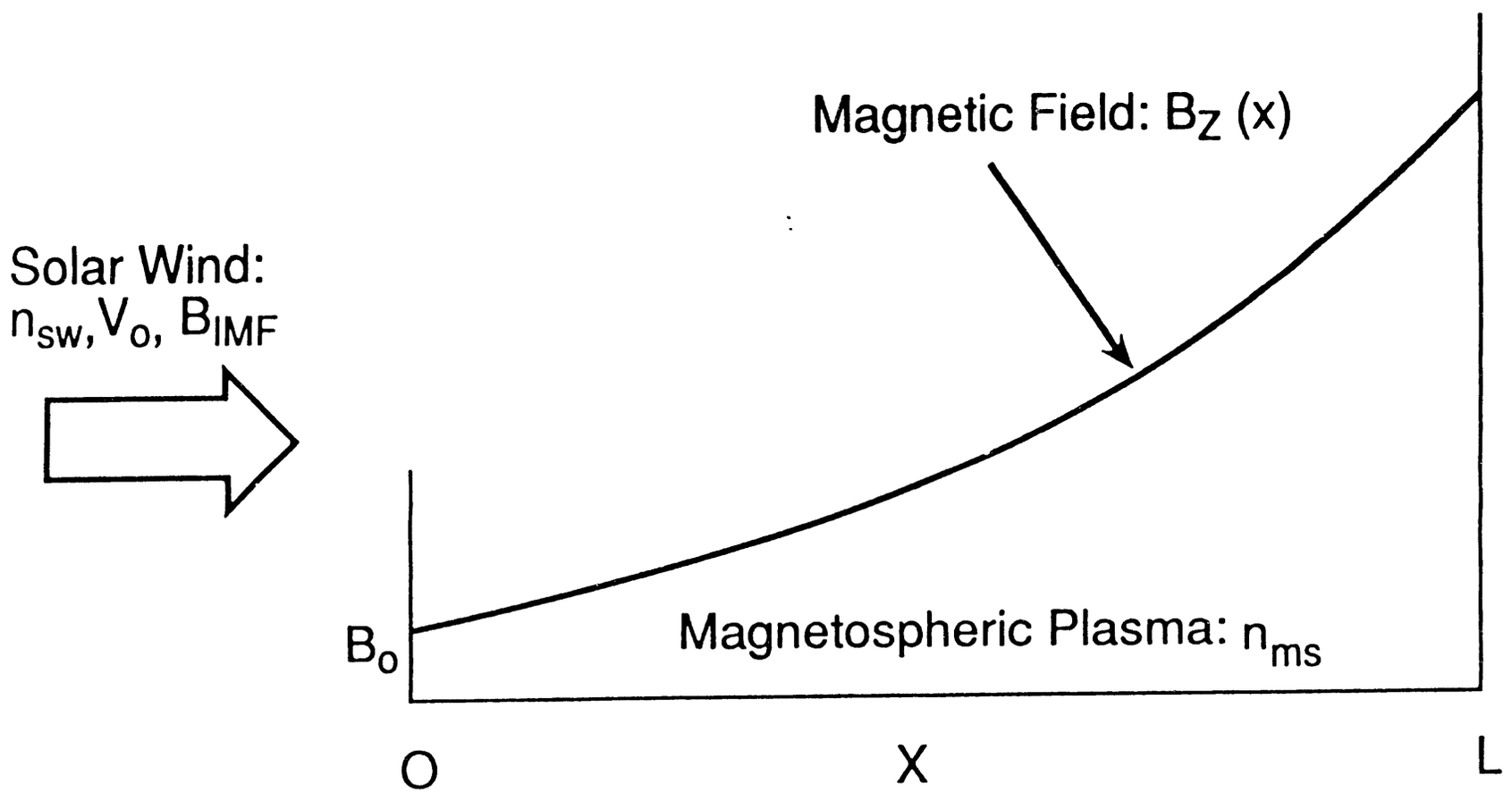
Magnetic Field: B_Z (x)
Solar Wind:
n_{sw}, V_o, B_{IMF}
B_o
Magnetospheric Plasma: n_{ms}
O
X
L

Fig. 1

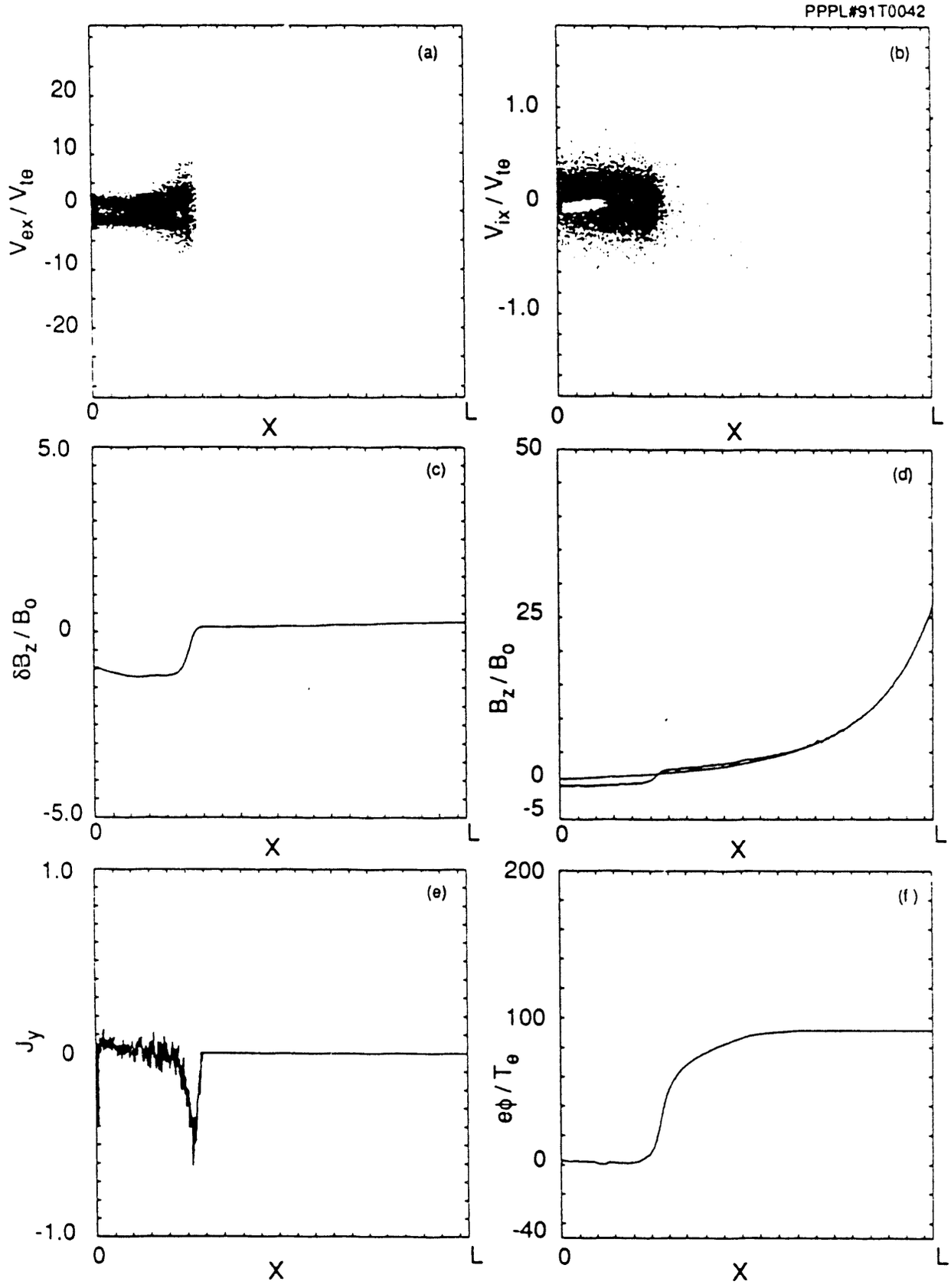
PPPL#91T0042
(a)
(b)
(c)
(d)
(e)
(f)
V_{ex} / V_{te}
V_{ix} / V_{te}
$\delta B_z / B_o$
B_z / B_o
J_y
$e\phi / T_e$
X
0
L

Fig. 2

PPPL#91T0043

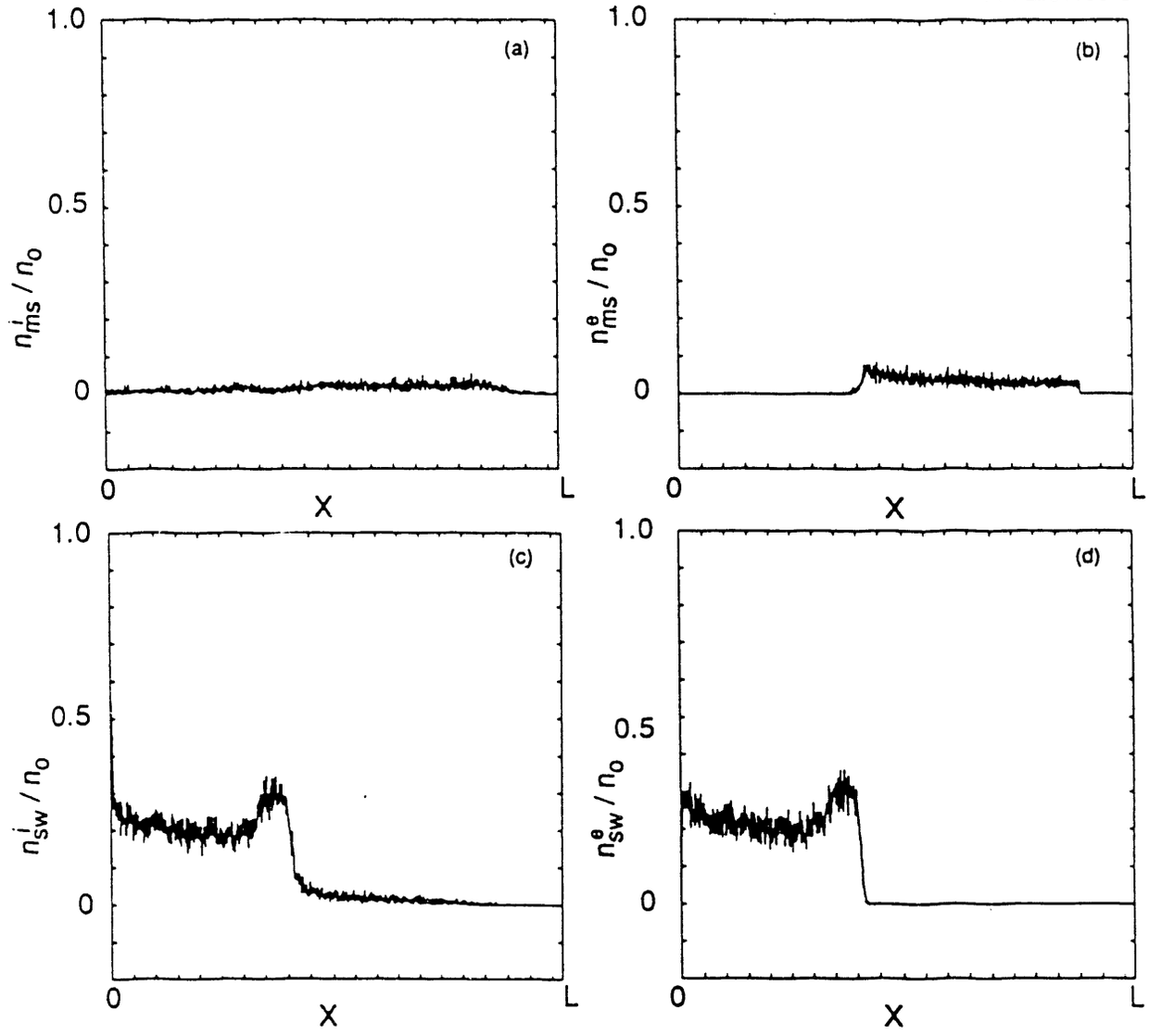

Fig. 3

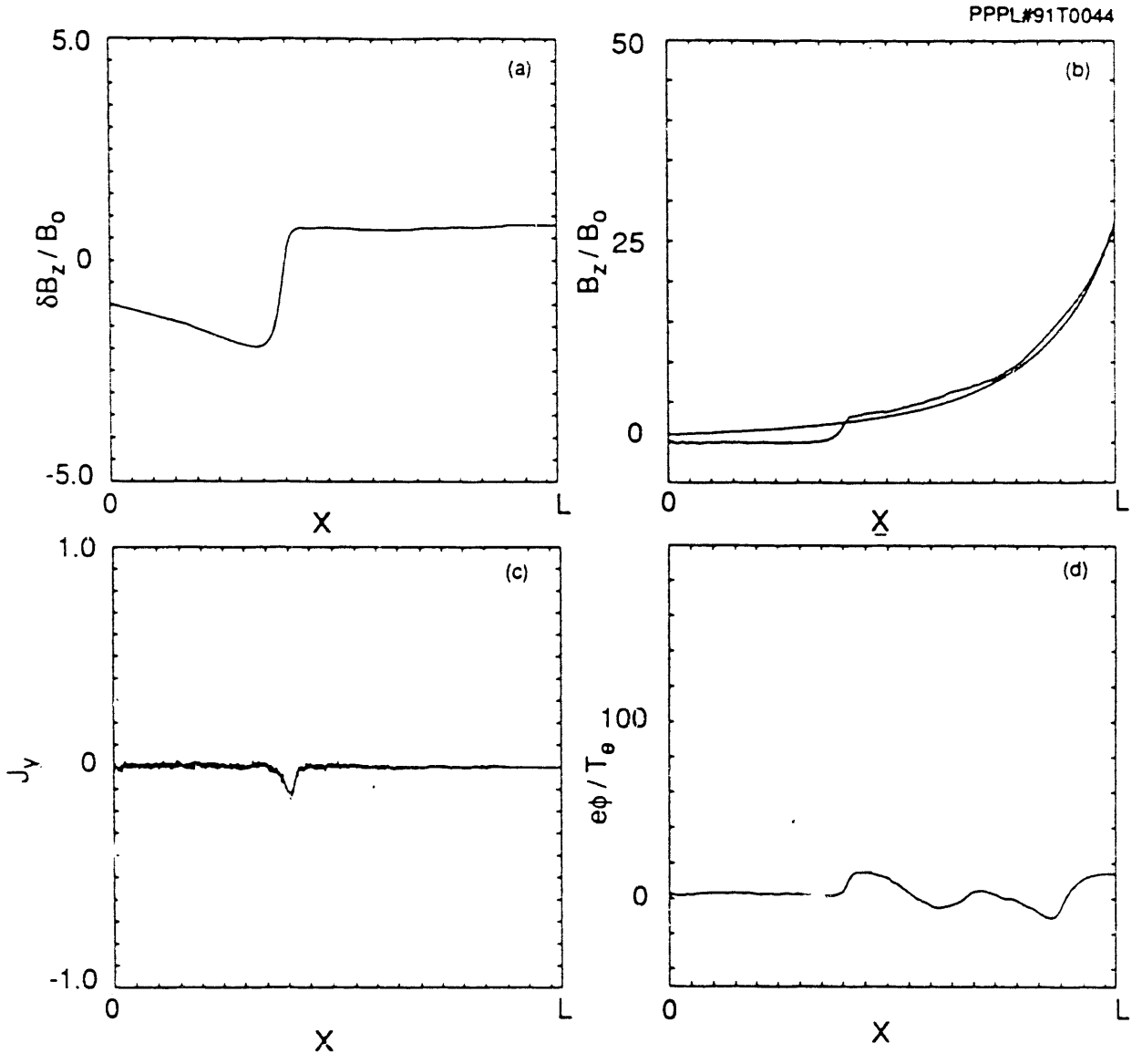
PPPL#91T0044
(a)
5.0
0
-5.0
δBz / Bo
0
X
L
(b)
50
25
0
Bz / Bo
0
X
L
(c)
1.0
0
-1.0
Jy
0
X
L
(d)
100
0
eφ / Te
0
X
L

Fig. 4

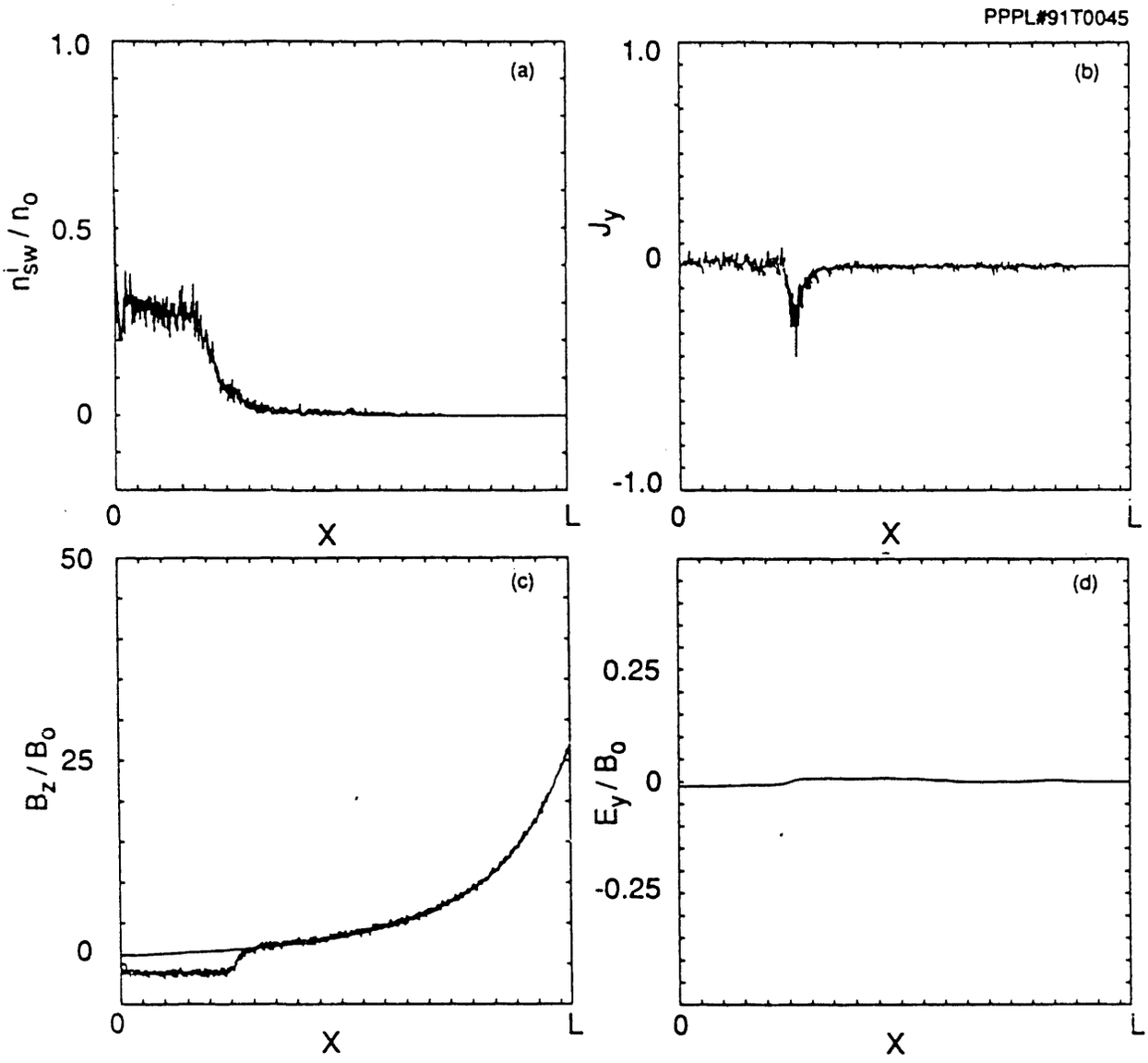
PPPL#91T0045
(a)
(b)
(c)
(d)
n^i_{sw} / n_o
J_y
B_z / B_o
E_y / B_o
1.0
0.5
0
-1.0
50
25
0.25
-0.25
0
X
L

Fig. 5

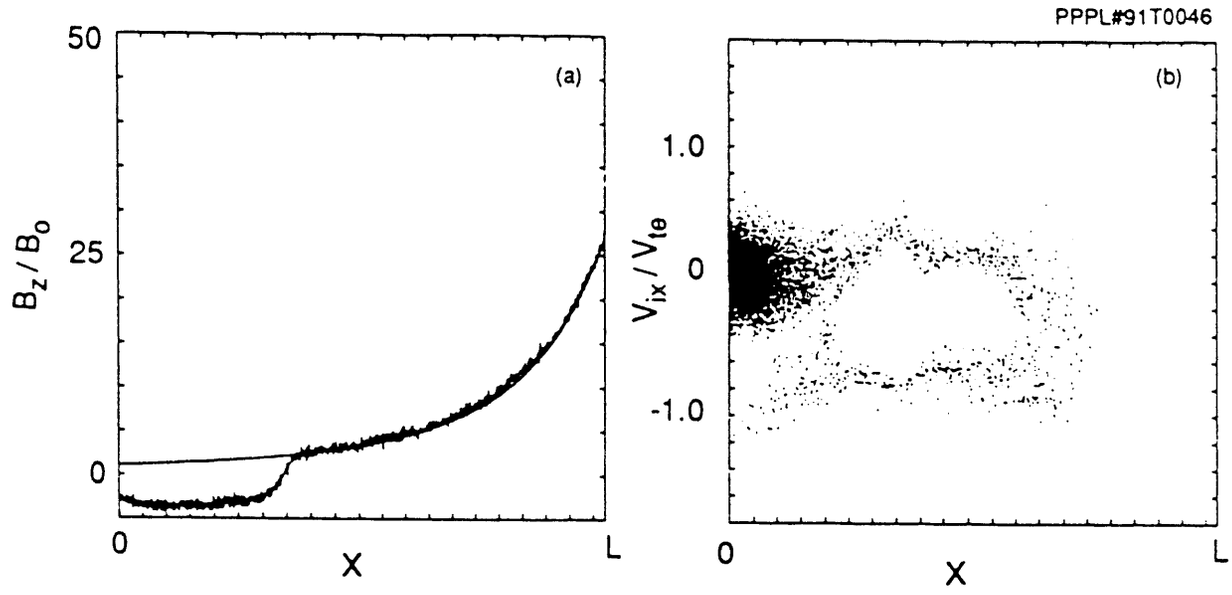

Fig. 6

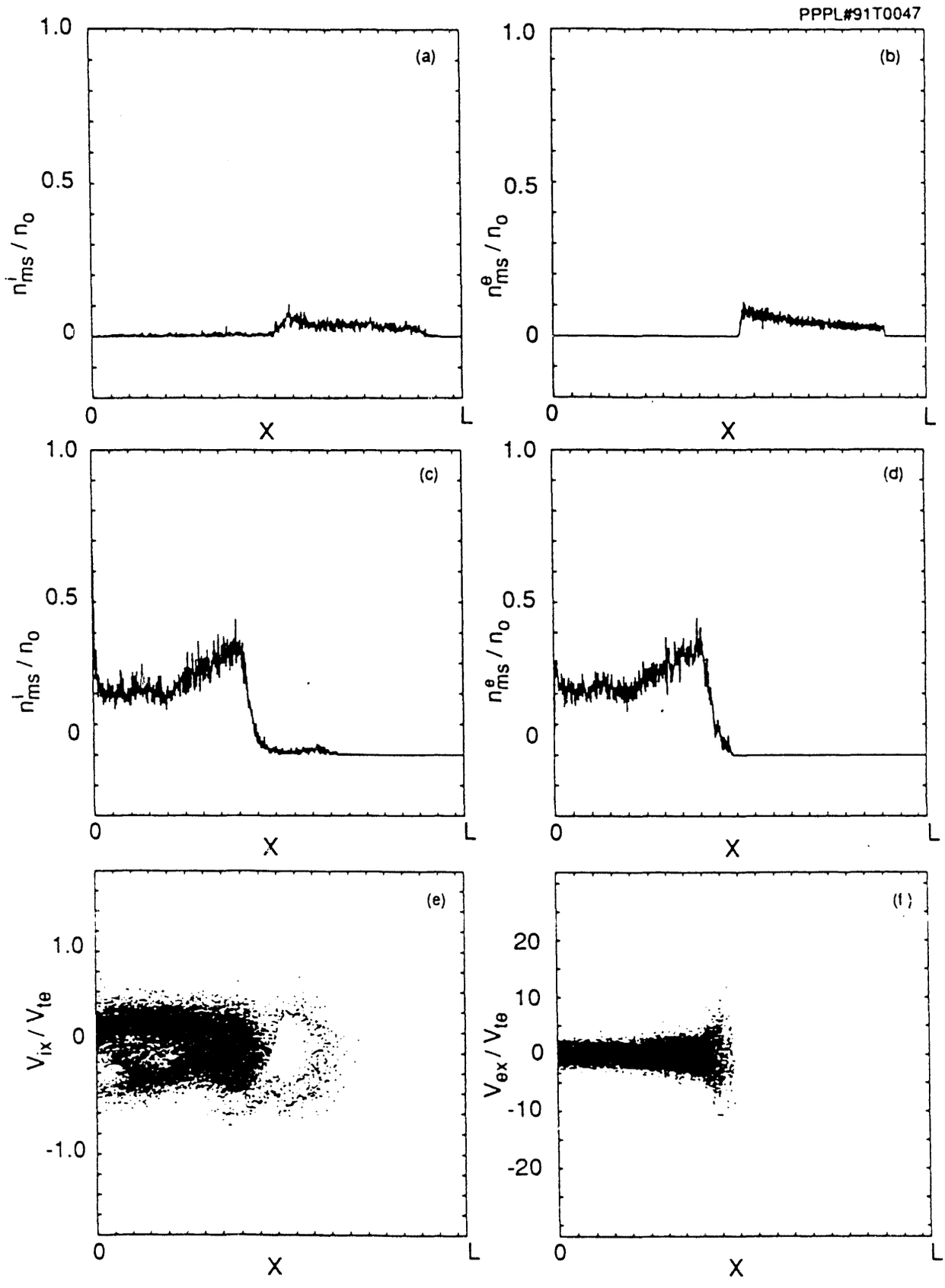
PPPL#91T0047
(a)
(b)
(c)
(d)
(e)
(f)
1.0
0.5
0
-1.0
20
10
-10
-20
X
L
n^i_{ms} / n_o
n^e_{ms} / n_o
V_{ix} / V_{te}
V_{ex} / V_{te}

Fig. 7

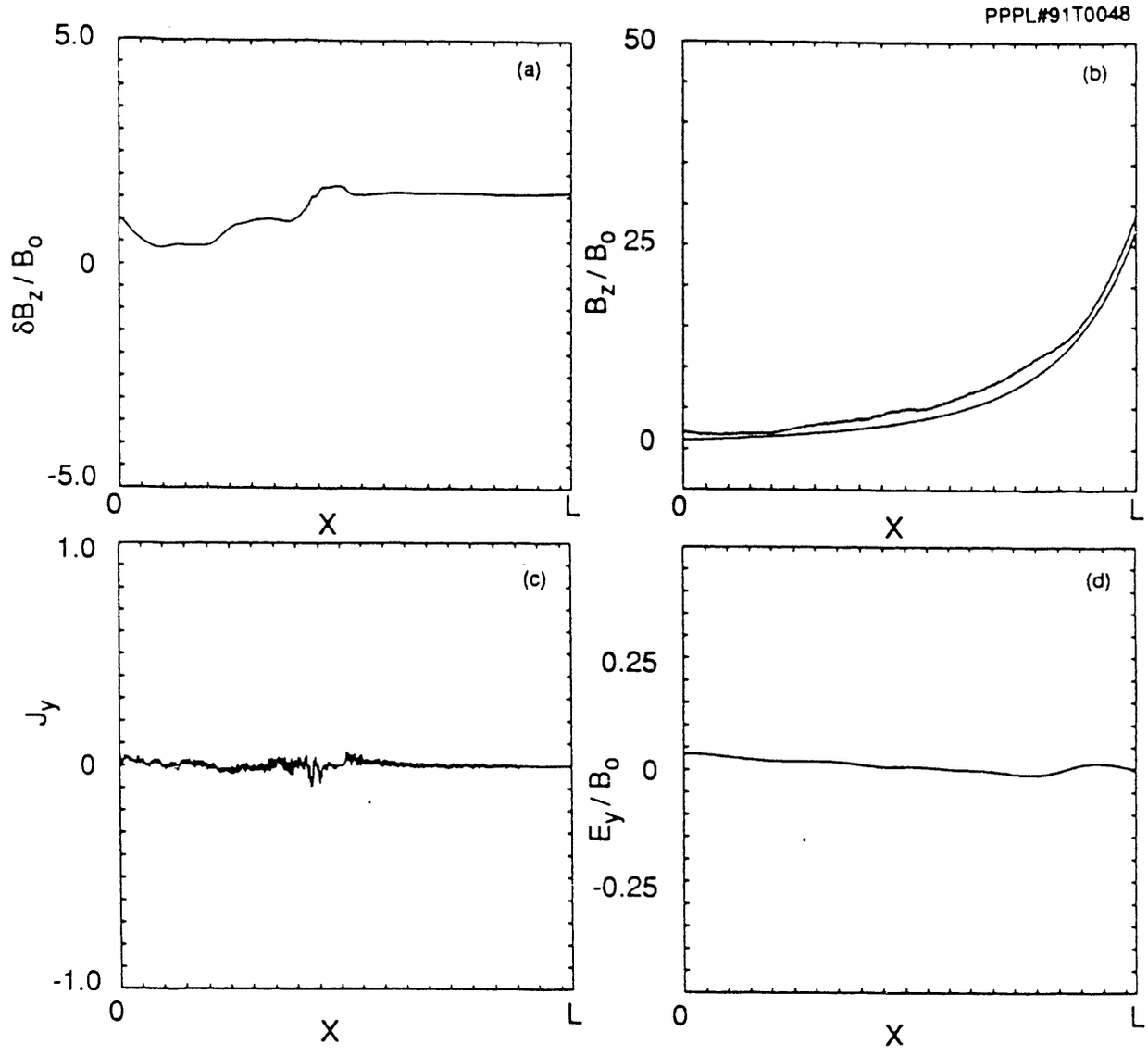
PPPL#91T0048
(a)
(b)
(c)
(d)
5.0
0
-5.0
$\delta B_z / B_o$
50
25
0
B_z / B_o
1.0
0
-1.0
J_y
0.25
0
-0.25
E_y / B_o
0
X
L

Fig. 8

EXTERNAL DISTRIBUTION IN ADDITION TO UC-420

Dr. F. Paoloni, Univ. of Wollongong, AUSTRALIA
Prof. M.H. Brennan, Univ. of Sydney, AUSTRALIA
Plasma Research Lab., Australian Nat. Univ., AUSTRALIA
Prof. I.R. Jones, Flinders Univ, AUSTRALIA
Prof. F. Cap, Inst. for Theoretical Physics, AUSTRIA
Prof. M. Heindler, Institut für Theoretische Physik, AUSTRIA
Prof. M. Goossens, Astronomisch Instituut, BELGIUM
Ecole Royale Militaire, Lab. de Phy. Plasmas, BELGIUM
Commission-European, DG. XII-Fusion Prog., BELGIUM
Prof. R. Boucique, Rijksuniversiteit Gent, BELGIUM
Dr. P.H. Sakanaka, Instituto Fisica, BRAZIL
Instituto De Pesquisas Espaciais-INPE, BRAZIL
Documents Office, Atomic Energy of Canada Ltd., CANADA
Dr. M.P. Bachynski, MPB Technologies, Inc., CANADA
Dr. H.M. Skarsgard, Univ. of Saskatchewan, CANADA
Prof. J. Teichmann, Univ. of Montreal, CANADA
Prof. S.R. Sreenivasan, Univ. of Calgary, CANADA
Prof. T.W. Johnston, INRS-Energie, CANADA
Dr. R. Bolton, Centre canadien de fusion magnétique, CANADA
Dr. C.R. James,, Univ. of Alberta, CANADA
Dr. P. Lukac, Komenskeho Universzita, CZECHOSLOVAKIA
The Librarian, Culham Laboratory, ENGLAND
Library, R61, Rutherford Appleton Laboratory, ENGLAND
Mrs. S.A. Hutchinson, JET Library, ENGLAND
P. Mähönen, Univ. of Helsinki, FINLAND
C. Mouttet, Lab. de Physique des Milieux Ionisés, FRANCE
J. Radet, CEN/CADARACHE - Bat 506, FRANCE
Ms. C. Rinni, Univ. of Ioannina, GREECE
Dr. T. Mual, Academy Bibliographic Ser., HONG KONG
Preprint Library, Hungarian Academy of Sci., HUNGARY
Dr. B. Das Gupta, Saha Inst. of Nuclear Physics, INDIA
Dr. P. Kaw, Inst. for Plasma Research, INDIA
Dr. P. Rosenau, Israel Inst. of Technology, ISRAEL
Librarian, International Center for Theo Physics, ITALY
Miss C. De Palo, Associazione EURATOM-ENEA , ITALY
Dr. G. Grosso, Istituto di Fisica del Plasma, ITALY
Dr. H. Yamato, Toshiba Res & Devel Center, JAPAN
Prof. I. Kawakami, Atomic Energy Res.Inst., JAPAN
Prof. K. Nishikawa, Hiroshima Univ., JAPAN
Director, Japan Atomic Energy Research Inst., JAPAN
Prof. S. Itoh, Kyushu Univ., JAPAN
Data and Planning Center, Nagoya Univ., JAPAN
Prof. S. Tanaka, Kyoto Univ., JAPAN
Library, Kyoto Univ., JAPAN
Prof. N. Inoue, Univ. of Tokyo, JAPAN
S. Mori, Technical Advisor, JAERI, JAPAN
O. Mitarai, Kumamoto Inst. of Technology, JAPAN
H. Jeong, Korea Advanced Energy Research Inst., KOREA
Prof. D.I. Choi, The Korea Adv. Inst. of Sci. & Tech., KOREA
Prof. B.S. Liley, Univ. of Waikato, NEW ZEALAND
Inst. of Plasma Physics, PEOPLE'S REPUBLIC OF CHINA
Librarian, Inst. of Physics, PEOPLE'S REPUBLIC OF CHINA
Library, Tsinghua Univ., PEOPLE'S REPUBLIC OF CHINA
Z. Li, S.W. Inst Physics, PEOPLE'S REPUBLIC OF CHINA
Prof. J.A.C. Cabral, Instituto Superior Tecnico, PORTUGAL
Dr. O. Petrus, AL I CUZA Univ., ROMANIA
Dr. J. de Villiers, Fusion Studies, AEC, S. AFRICA
Prof. M.A. Hellberg, Univ. of Natal, S. AFRICA
C.I.E.M.A.T, Fusion Division Library, SPAIN
Dr. L. Stenflo, Univ. of UMEA, SWEDEN
Library, Royal Inst. of Technology, SWEDEN
Prof. H. Wilhelmson, Chalmers Univ. of Tech., SWEDEN
Centre Phys. Des Plasmas, Ecole Polytech, SWITZERLAND
Bibliotheek, Inst. Voor Plasma-Fysica, THE NETHERLANDS
M. Durgut, Vice Chairman, Middle East Tech. Univ., TURKEY
Dr. D.D. Ryutov, Siberian Branch of Academy of Sci., USSR
Dr. G.A. Eliseev, Kurchatov Inst., USSR
Librarian, The Ukr.SSR Academy of Sciences, USSR
Dr. L.M. Kovrizhnykh, Inst. of General Physics, USSR
Kernforschungsanlage GmbH, Zentralbibliothek, W. GERMANY
Bibliothek, Inst. Für Plasmaforschung, W. GERMANY
Prof. K. Schindler, Ruhr-Universität Bochum, W. GERMANY
Dr. F. Wagner, (ASDEX), Max-Planck-Institut, W. GERMANY
Librarian, Max-Planck-Institut, W. GERMANY
Prof. R.K. Janev, Inst. of Physics, YUGOSLAVIA

END

DATE FILMED

01/09/92